Hindawi
Shock and Vibration
Volume 2019, Article ID 1648709, 15 pages
https://doi.org/10.1155/2019/1648709

Research Article

Evaluation Method for Vibration Measurement on Casing in Aeroengine: Theoretical Analysis and Experimental Study

Lanlan Hou[1,2,3] **and Shuqian Cao**[1,2,3]

[1]*Department of Mechanics, Tianjin University, Tianjin 300354, China*
[2]*Tianjin Key Laboratory of Nonlinear Dynamics and Control, Tianjin 300354, China*
[3]*National Demonstration Center for Experimental Mechanics Education (Tianjin University), Tianjin 300354, China*

Correspondence should be addressed to Shuqian Cao; sqcao@tju.edu.cn

Received 3 December 2018; Accepted 14 February 2019; Published 14 March 2019

Academic Editor: Fiorenzo A. Fazzolari

The vibration measurement location is the basis for effective monitoring of aeroengine vibration conditions. Measurement locations need to reflect the vibration of the rotor sufficiently, while complex structures of the aeroengine bring many excitation sources. This paper presents an evaluation methodology for vibration measurement on casing in the aeroengine. A number of indexes are defined to quantify and characterize the vibration measurement ability of main measurement locations on casing for rotor vibration. A dynamic model of a dual-rotor-casing system is established according to the support structure of a certain type of aeroengine. By means of the introduced evaluation method, the vibration relation between rotors and the main vibration measurement sections is analyzed. Response characteristics and performance orders of measurement sections are given. The rationality of theoretical results is sound verified by experiments on a designed pneumatic-driven double-rotor-casing test bench. The best measured vibration section is consistent with the actual on-board vibration section of the engine, which further demonstrates the effectiveness of the evaluation method. The research results can provide a basis for the selection and optimization of vibration measurement locations and fault diagnosis in the aeroengine. Furthermore, the application of this method is not limited to aeroengine vibration analysis and sensor measurement location optimization, but will be useful for vibration analysis of other rotating machinery.

1. Introduction

Vibration monitoring is a necessary mean to ensure safety and reliability for aeroengine. An ultimate goal of vibration monitoring is to maximize the amount of meaningful information which can be extracted from disparate data sources to obtain comprehensive diagnostic and prognostic knowledge regarding the health of the engine. Aeroengine data are available from a variety of sources including on-board sensor measurements. The challenge of how to evaluate and select measurement locations has become imperative.

The vibration of the aeroengine is extremely complicated caused by numerous and complex structures and harsh operation environments. It is difficult to monitor the vibration of all structural components of the whole machine. The vibration monitoring is currently mainly aimed at the core component of the aeroengine (the rotor system).

In the dual-rotor configuration of turbofan engine rotor systems, the bearing frame, compressor stator, turbine stator, and other casings form the main stator frame of the engine. The high-pressure compressor and the high-pressure turbine are connected together through a hollow shaft to form a high-pressure rotor. The low-pressure shaft passes through the high-pressure shaft to connect the low-pressure compressor with the low-pressure turbine to form a low-pressure rotor. The high- and low-pressure shafts need to ensure a certain degree of concentricity. The high- and the low-pressure rotors are installed in the engine through the bearing housing, and intermediate bearings may also be used between the two rotors. The engine is fixed to the aircraft or test bed through a main mount and an auxiliary mount on the engine casing.

The casing is the main component for implementing the vibration monitoring of the whole engine. Since the aeroengine rotor runs at a high speed inside the engine casing, it is necessary to indirectly measure the rotor vibration through vibration sensors on the casing. Researchers installed sensors close to the bearing support section for vibration monitoring of the CH-47D [1] to minimize the energy attenuation of the rotor vibration transmitted to the casing vibration point. It is generally believed that the vibration measurement section is mainly selected according to the casing section of the supporting bearing.

For a certain type of aeroengine, the test-bed vibration measurement sections include front, middle, and rear sections, which correspond to the bearing support positions of the front casing, the intermediate casing, and the rear casing. The on-board vibration measurement locations should be no more than two and mainly selected from the measurement sections on test bed. In addition, the number of vibration monitoring channels for the main part is approximately 2–6 sensors. For example, the F100-PW-200 engine has 4 acceleration sensors installed on the casing to monitor vibration [2]. Therefore, how to reasonably choose the vibration measurement section and arrange the sensors becomes a key issue for measured vibration signal fully reflecting the structural vibration and fault condition.

In the current researches, the vibration sensor-optimized layout method and effectiveness of vibration measurement points are studied based on fault frequency sensitivity, rotor support form, and vibration transmission path for the selection of vibration sensor installation position [3, 4]. Ouyang et al. [5] proposed an optimization principle of the surface measurement points on casing according to vibration measurement requirements of the aeroengine vibration sensor. The effectiveness of the screening principle including vibration amplitude mean value and peak screening was verified by simulation analysis. Wang et al. [6] proposed a vibration sensor layout scheme based on the vibration sensor specification of an engine overall scheme and proposed a comprehensive evaluation index to serve the layout optimization of the engine vibration sensor.

Placing vibration sensors at appropriate locations plays an important role in engineering; some methods have already been proposed in literatures [7, 8]. Li et al. [9] proposed a novel sensor placement criterion for structural health monitoring with the objective of best identification of modal frequencies and mode shapes. The method was derived by the representative least squares. Cherng [10] systematically analyzed existing methods and proposed methods that either improve their performance or accelerate the searching process for modal parameter identification. The approach used was based on the analytical formulation of singular value decomposition.

The use of optimization techniques for choosing sensor locations has been the subject of a number of researches [11–13]. Sensmeier and Nichol [14] developed a methodology by genetic algorithm for determining optimum sensor locations for measuring vibratory response of a single blade in the turbine engine. Xu et al. [15] proposed a sensor selection approach for an aircraft gas turbine engine and showed its effectivity numerically. Najjar et al. [16] gave an optimal sensor set selection that contains the most relevant information for fault classification in a two-step process for fouling diagnosis of the heat exchanger of an aircraft. Tapken and Enghardt [17] conducted a systematic numerical study of the optimization of sensor arrangements for induct radial mode analysis at high frequencies.

The vibration measurement of aeroengines is affected not only by the sensor installation structure and engine operating conditions but also the complex casing structure and restricted measurement locations and orientation. How to collect the vibration data through the limited vibration measurement locations of the whole engine and accurately reflect the vibration level and fault of the internal rotor is the subject on the optimization of the vibration sensor layout in aeroengines.

The arrangement of vibration measurement locations in engineering is basically determined in terms of inheritance and reference. The selection of the vibration measurement locations and determination of the measurement location combination are based on exploration and verification for a certain engine. However, there are few related researches about how to explore, verify, evaluate, and improve the vibration measurement layout. To fix this problem, this paper proposes a research method to evaluate the vibration measurement of casing based on an established dual-rotor-casing system by defining a series of vibration evaluation indexes. Furthermore, the effectiveness of the method is verified by theoretical and experimental simulation by developing a pneumatic-driven double-rotor-casing test bench.

2. Method for Vibration Measurement Evaluation on Casing in Aeroengine

Generally, acceleration sensors are mounted on the aeroengine casing to measure vibration. The vibration is transferred to the casing through different transfer paths. The vibration signal measured on the casing is a result of the combined modulation from many vibration components, such as the unbalanced response of the low- and high-pressure rotors, the misalignment response of low-pressure rotor, and the vibration response of bearings. The vibration relation between rotors and the main measurement locations becomes an object of this study. An evaluation method is given, and several indexes are defined in this section.

2.1. Method for Vibration Measurement Evaluation on Casing. According to the development trend of aeroengine vibration measurement, the vibration measurement target is to use as few sensors as possible to reflect as much vibration information as possible. Therefore, it is necessary to evaluate the comprehensive vibration measurement ability of the casing vibration measurement section, so that the sensor layout scheme can meet the vibration measurement target.

The evaluation of the vibration measurement ability needs to determine the evaluation index first and then establish the dynamic model of the rotor-casing system, and calculate

dynamic responses. Based on dynamic characteristics, the specific evaluation index of the main vibration measurement section on the casing can be obtained to reflect the characteristics of rotor vibration. Combining with the analysis of experimental data, the comprehensively vibration measurement ability of vibration measurement sections will be addressed, and the ability order of vibration measurement shall be given. Finally, the on-board measurement location can be selected based on the better vibration measurement section. The flowchart of the aforementioned evaluation method of vibration measurement on casing is shown in Figure 1.

2.2. Evaluation Index for Vibration Measurement Section. The evaluation indexes from the research method include vibration transmissibility, energy transmissibility, response relativity, vibration sensitivity, and vibration measurement ability. These indexes provide an excellent way to view the general vibration characteristics of the system from a macroscopic perspective.

2.2.1. Vibration Transmissibility. The vibration from rotor to casing goes through multiple components and transfer paths. In order to characterize the vibration transmission of the rotor system, the vibration transmissibility ξ_{ij} is introduced and defined as the response amplitude ratio between two vibration components, as shown in equation (1). The root mean square (RMS) is used to characterize the average amplitude of the response [18]. The response RMS value at a certain speed is calculated by equation (2), where J is the total number of response data points [19]:

$$\xi_{ij} = \frac{\mathrm{RMS}_i}{\mathrm{RMS}_j}, \tag{1}$$

$$\mathrm{RMS}_j = \sqrt{\frac{1}{J}\sum_{j=1}^{J} a_j^2}. \tag{2}$$

2.2.2. Energy Transmissibility. The energy transmissibility η_{ij} is defined as the ratio of vibration energy between two components, as shown in equation (3). The vibration energy of the ith components in an excitation cycle is expressed in the following equations:

$$\eta_{ij} = \frac{E_i}{E_j}, \tag{3}$$

$$E_i = \int_0^T \dot{x}_i^2 dt. \tag{4}$$

According to the vibration transfer direction, the vibration data of receiving ends are generally used as the numerator of the transmissibility, while the vibration data of vibration sources are used as the denominator of the transmissibility. For example, the vibration transmissibility and energy transmissibility of disk to bearing in the rotor-casing is

$$\xi_{\mathrm{db}} = \frac{\mathrm{RMS}_{\mathrm{b}}}{\mathrm{RMS}_{\mathrm{d}}}, \qquad \eta_{\mathrm{db}} = \frac{E_{\mathrm{b}}}{E_{\mathrm{d}}}. \tag{5}$$

2.2.3. Response Relativity. The vibration data collected at measurement locations need to reflect the vibration of internal components in the rotor system as much as possible. Among them, the vibration of the rotor is the most important excitation source. The response relativity $R(x_{\mathrm{s}}, x_{\mathrm{r}})$ is used to characterize the vibration relation between the response x_{s} of the measurement location and the response x_{r} of the rotor:

$$R(x_{\mathrm{s}}, x_{\mathrm{r}}) = \frac{\mathrm{Cov}(x_{\mathrm{s}}, x_{\mathrm{r}})}{\sqrt{\mathrm{Var}[x_{\mathrm{s}}]\mathrm{Var}[x_{\mathrm{r}}]}}, \tag{6}$$

where $\mathrm{Cov}(x_{\mathrm{s}}, x_{\mathrm{r}})$ is the covariance of x_{s} and x_{r}, $\mathrm{Var}[x_{\mathrm{s}}]$ is the variance of x_{s}, and $\mathrm{Var}[x_{\mathrm{r}}]$ is the variance of x_{r}.

2.2.4. Vibration Sensitivity. There are many internal excitation sources in the rotor system, and the casing brings interference, which makes the frequency of the vibration response from the measurement location complex. The vibration sensitivity S, a frequency domain index, is defined to describe the proportion of the rotor vibration characteristic frequency in the response of the measurement location. In the response of the measurement location, S equals the ratio of the amplitude of the internal characteristic frequency (such as the fundamental frequency and the fault frequency) to the amplitudes sum of all frequencies:

$$S = \frac{A_{f_{\mathrm{ch}}}}{\sum_{m=1}^{M} A_{f_m}}, \tag{7}$$

where $A_{f_{\mathrm{ch}}}$ is the amplitude of the characteristic frequency, A_{f_m} is the amplitude of the mth frequency in the measurement response, and M is the number of frequency components.

2.2.5. Vibration Measurement Ability. After knowing the characteristics and focus of each measurement location, it is necessary to comprehensively evaluate the vibration measurement ability of the measurement location. The comprehensive measurement ability C is defined to characterize its ability to reflect the internal vibration:

$$C = p_1\overline{\xi} + p_2\overline{\eta} + p_3\overline{R} + p_4\overline{S}, \tag{8}$$

where $\overline{*}$ represents the ratio between the value of the variable $*$ at each speed and the mean over the full speed band. p_1, p_2, p_3, and p_4 are weighting factors determined according to the purpose of vibration measurement and monitoring requirements.

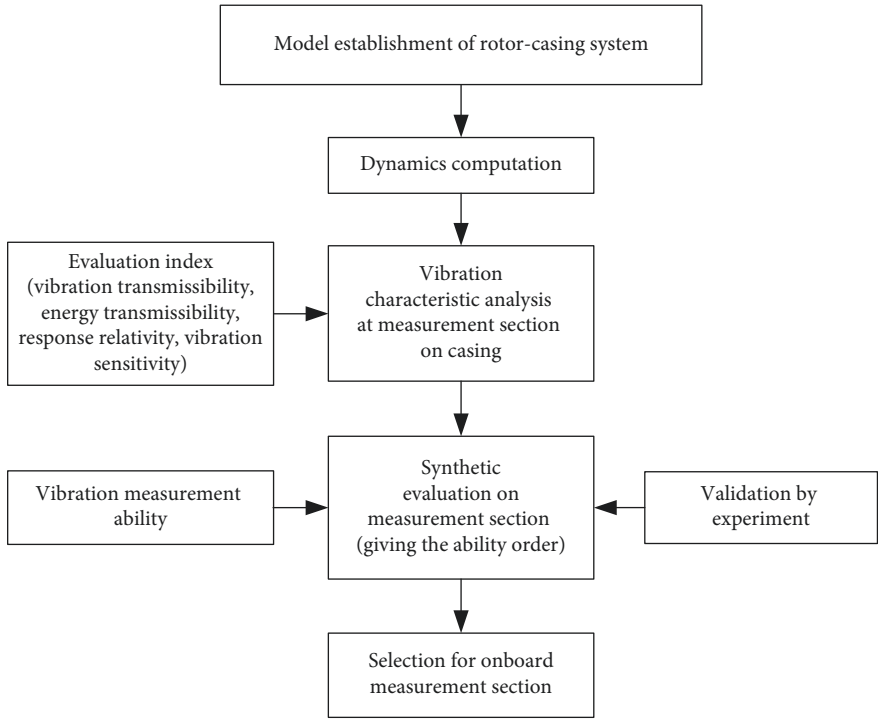

Figure 1: Flowchart of evaluation method for vibration measurement on casing.

3. Modelling of a Dual-Rotor-Casing System

In order to verify the effectiveness of the proposed evaluation method, the dynamic model of a dual-rotor-casing system is established according to the configuration of a certain aeroengine rotor system, as shown in Figure 2. Based on the lumped parameter theory, the high-pressure rotor is simplified into a disc and a massless shaft. The mass is concentrated on disk and both ends of the rotating shaft. The inner race of bearings and the end of the rotating shaft are integrated into one body. The low-pressure rotor is simplified into two parts connected by a coupling which do not transfer transverse vibration. The two rotors are coupled together via an intermediate bearing 5, and each has an unbalanced excitation. The casing is bolted with tangential stiffness and damping. Bearings 1, 3, 5, and 6 are roller bearings, and bearings 2 and 4 are angular contact ball bearings.

According to Newton's second law, the system differential equations of all the components can be established as follows:

High-pressure disc:

$$\begin{aligned} &m_{\mathrm{hd}}\ddot{x}_{\mathrm{hd}} + c_{\mathrm{hd}}\dot{x}_{\mathrm{hd}} + k_{\mathrm{hs}}\left(x_{\mathrm{hd}} - x_{\mathrm{hb4}}\right) + k_{\mathrm{hs}}\left(x_{\mathrm{hd}} - x_{\mathrm{hb5}}\right) \\ &\quad = m_{\mathrm{hd}}e_{\mathrm{h}}\omega_{\mathrm{h}}^2\cos\left(\omega_{\mathrm{h}}t\right), \\ &m_{\mathrm{hd}}\ddot{y}_{\mathrm{hd}} + c_{\mathrm{hd}}\dot{y}_{\mathrm{hd}} + k_{\mathrm{hs}}\left(y_{\mathrm{hd}} - y_{\mathrm{hb4}}\right) + k_{\mathrm{hs}}\left(y_{\mathrm{hd}} - y_{\mathrm{hb5}}\right) \\ &\quad = m_{\mathrm{hd}}e_{\mathrm{h}}\omega_{\mathrm{h}}^2\sin\left(\omega_{\mathrm{h}}t\right) - m_{\mathrm{hd}}g. \end{aligned} \tag{9}$$

Inner race of bearing 4:

$$\begin{aligned} &m_{\mathrm{hb4}}\ddot{x}_{\mathrm{hb4}} + c_{\mathrm{hb4}}\left(\dot{x}_{\mathrm{hb4}} - \dot{x}_{\mathrm{b4}}\right) + k_{\mathrm{hs}}\left(x_{\mathrm{hb4}} - x_{\mathrm{hd}}\right) \\ &\quad - F_{\mathrm{hb4}x} = 0, \\ &m_{\mathrm{hb4}}\ddot{y}_{\mathrm{hb4}} + c_{\mathrm{hb4}}\left(\dot{y}_{\mathrm{hb4}} - \dot{y}_{\mathrm{b4}}\right) + k_{\mathrm{hs}}\left(y_{\mathrm{hb4}} - y_{\mathrm{hd}}\right) \\ &\quad - F_{\mathrm{hb4}y} = -m_{\mathrm{hb4}}g. \end{aligned} \tag{10}$$

Out race of bearing 5:

$$\begin{aligned} &m_{\mathrm{hb5}}\ddot{x}_{\mathrm{hb5}} + c_{\mathrm{hb5}}\left(\dot{x}_{\mathrm{hb5}} - \dot{x}_{\mathrm{lb5}}\right) + k_{\mathrm{hs}}\left(x_{\mathrm{hb5}} - x_{\mathrm{hd}}\right) \\ &\quad + F_{\mathrm{lb5}x} = 0, \\ &m_{\mathrm{hb5}}\ddot{y}_{\mathrm{hb5}} + c_{\mathrm{hb5}}\left(\dot{y}_{\mathrm{hb5}} - \dot{y}_{\mathrm{lb5}}\right) + k_{\mathrm{hs}}\left(y_{\mathrm{hb5}} - y_{\mathrm{hd}}\right) \\ &\quad + F_{\mathrm{lb5}y} = -m_{\mathrm{hb5}}g. \end{aligned} \tag{11}$$

Low-pressure disc 1:

$$\begin{aligned} &m_{\mathrm{ld1}}\ddot{x}_{\mathrm{ld1}} + c_{\mathrm{l1}}\dot{x}_{\mathrm{ld1}} + k_{\mathrm{l1}}\left(x_{\mathrm{ld1}} - x_{\mathrm{lb1}}\right) + k_{\mathrm{l1}}\left(x_{\mathrm{ld1}} - x_{\mathrm{lb2}}\right) \\ &\quad = m_{\mathrm{ld1}}e_{\mathrm{l1}}\omega_{\mathrm{l}}^2\cos\left(\omega_{\mathrm{l}}t\right), \\ &m_{\mathrm{ld1}}\ddot{y}_{\mathrm{ld1}} + c_{\mathrm{l1}}\dot{y}_{\mathrm{ld1}} + k_{\mathrm{l1}}\left(y_{\mathrm{ld1}} - y_{\mathrm{lb1}}\right) + k_{\mathrm{l1}}\left(y_{\mathrm{ld1}} - y_{\mathrm{lb2}}\right) \\ &\quad = m_{\mathrm{ld1}}e_{\mathrm{l1}}\omega_{\mathrm{l}}^2\sin\left(\omega_{\mathrm{l}}t\right) - m_{\mathrm{ld1}}g. \end{aligned} \tag{12}$$

Inner race of bearing 1:

$$\begin{aligned} &m_{\mathrm{lb1}}\ddot{x}_{\mathrm{lb1}} + c_{\mathrm{lb1}}\left(\dot{x}_{\mathrm{lb1}} - \dot{x}_{\mathrm{b1}}\right) + k_{\mathrm{l1}}\left(x_{\mathrm{lb1}} - x_{\mathrm{ld1}}\right) \\ &\quad - F_{\mathrm{lb1}x} = 0, \\ &m_{\mathrm{lb1}}\ddot{y}_{\mathrm{lb1}} + c_{\mathrm{lb1}}\left(\dot{y}_{\mathrm{lb1}} - \dot{y}_{\mathrm{b1}}\right) + k_{\mathrm{l1}}\left(y_{\mathrm{lb1}} - y_{\mathrm{ld1}}\right) \\ &\quad - F_{\mathrm{lb1}y} = -m_{\mathrm{lb1}}g. \end{aligned} \tag{13}$$

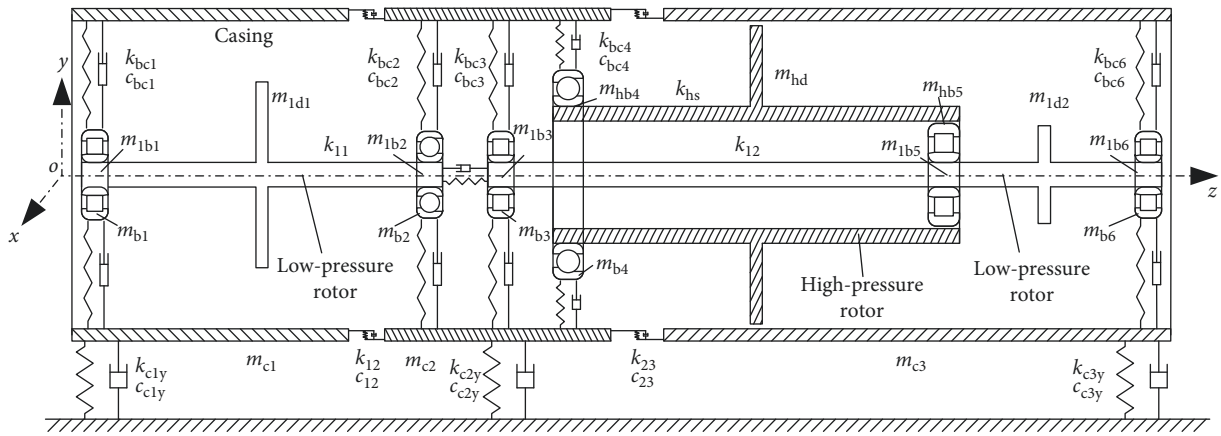

Figure 2: Dynamic model of dual-rotor-casing system.

Inner race of bearing 2:

$$\begin{aligned} &m_{lb2}\ddot{x}_{lb2} + c_{lb2}\left(\dot{x}_{lb2} - \dot{x}_{b2}\right) + k_{l1}\left(x_{lb2} - x_{ld1}\right) \\ &\quad - F_{lb2x} = 0, \\ &m_{lb2}\ddot{y}_{lb2} + c_{lb2}\left(\dot{y}_{lb2} - \dot{y}_{b2}\right) + k_{l1}\left(y_{lb2} - y_{ld1}\right) \\ &\quad - F_{lb2y} = -m_{lb2}g. \end{aligned} \tag{14}$$

Low-pressure disc 2:

$$\begin{aligned} &m_{ld2}\ddot{x}_{ld2} + c_{l2}\dot{x}_{ld2} + k_{l2}\left(x_{ld2} - x_{lb3}\right) + k_{l2}\left(x_{ld2} - x_{lb5}\right) \\ &\quad = m_{ld2}e_{l2}\omega_1^2\cos\left(\omega_1 t\right), \\ &m_{ld2}\ddot{y}_{ld2} + c_{l2}\dot{y}_{ld2} + k_{l2}\left(y_{ld2} - y_{lb3}\right) + k_{l2}\left(y_{ld2} - y_{lb5}\right) \\ &\quad = m_{ld2}e_{l2}\omega_1^2\sin\left(\omega_1 t\right) - m_{ld2}g. \end{aligned} \tag{15}$$

Inner race of bearing 3:

$$\begin{aligned} &m_{lb3}\ddot{x}_{lb3} + c_{lb3}\left(\dot{x}_{lb3} - \dot{x}_{b3}\right) + k_{l2}\left(x_{lb3} - x_{ld2}\right) \\ &\quad - F_{lb3x} = 0, \\ &m_{lb3}\ddot{y}_{lb3} + c_{lb3}\left(\dot{y}_{lb3} - \dot{y}_{b3}\right) + k_{l2}\left(y_{lb3} - y_{ld2}\right) \\ &\quad - F_{lb3y} = -m_{lb3}g. \end{aligned} \tag{16}$$

Inner race of bearing 5:

$$\begin{aligned} &m_{lb5}\ddot{x}_{lb5} + c_{hb5}\left(\dot{x}_{lb5} - \dot{x}_{hb5}\right) + k_{l2}\left(x_{lb5} - x_{ld2}\right) \\ &\quad + k_{l2}\left(x_{lb5} - x_{lb6}\right) - F_{lb5x} = 0, \\ &m_{lb5}\ddot{y}_{lb5} + c_{hb5}\left(\dot{y}_{lb5} - \dot{y}_{hb5}\right) + k_{l2}\left(y_{lb5} - y_{ld2}\right) \\ &\quad + k_{l2}\left(y_{lb5} - y_{lb6}\right) - F_{lb5y} = -m_{lb5}g. \end{aligned} \tag{17}$$

Inner race of bearing 6:

$$\begin{aligned} &m_{lb6}\ddot{x}_{lb6} + c_{lb6}\left(\dot{x}_{lb6} - \dot{x}_{b6}\right) + k_{l2}\left(x_{lb6} - x_{lb5}\right) \\ &\quad - F_{lb6x} = 0, \\ &m_{lb6}\ddot{y}_{lb6} + c_{lb6}\left(\dot{y}_{lb6} - \dot{y}_{b6}\right) + k_{l2}\left(y_{lb6} - y_{lb5}\right) \\ &\quad - F_{lb6y} = -m_{lb6}g. \end{aligned} \tag{18}$$

Out race of bearing 1:

$$\begin{aligned} &m_{b1}\ddot{x}_{b1} + c_{lb1}\left(\dot{x}_{b1} - \dot{x}_{lb1}\right) + c_{bc1}\left(\dot{x}_{b1} - \dot{x}_{c1}\right) \\ &\quad + k_{bc1}\left(x_{b1} - x_{c1}\right) + F_{lb1x} = 0, \\ &m_{b1}\ddot{y}_{b1} + c_{lb1}\left(\dot{y}_{b1} - \dot{y}_{lb1}\right) + c_{bc1}\left(\dot{y}_{b1} - \dot{y}_{c1}\right) \\ &\quad + k_{bc1}\left(y_{b1} - y_{c1}\right) + F_{lb1y} = -m_{b1}g. \end{aligned} \tag{19}$$

Out race of bearing 2:

$$\begin{aligned} &m_{b2}\ddot{x}_{b2} + c_{lb2}\left(\dot{x}_{b2} - \dot{x}_{lb2}\right) + c_{bc2}\left(\dot{x}_{b2} - \dot{x}_{c2}\right) \\ &\quad + k_{bc2}\left(x_{b2} - x_{c2}\right) + F_{lb2x} = 0, \\ &m_{b2}\ddot{y}_{b2} + c_{lb2}\left(\dot{y}_{b2} - \dot{y}_{lb2}\right) + c_{bc2}\left(\dot{y}_{b2} - \dot{y}_{c2}\right) \\ &\quad + k_{bc2}\left(y_{b2} - y_{c2}\right) + F_{lb2y} = -m_{b2}g. \end{aligned} \tag{20}$$

Out race of bearing 3:

$$\begin{aligned} &m_{b3}\ddot{x}_{b3} + c_{lb3}\left(\dot{x}_{b3} - \dot{x}_{lb3}\right) + c_{bc3}\left(\dot{x}_{b3} - \dot{x}_{c2}\right) \\ &\quad + k_{bc3}\left(x_{b3} - x_{c2}\right) + F_{lb3x} = 0, \\ &m_{b3}\ddot{y}_{b3} + c_{lb3}\left(\dot{y}_{b3} - \dot{y}_{lb3}\right) + c_{bc3}\left(\dot{y}_{b3} - \dot{y}_{c2}\right) \\ &\quad + k_{bc3}\left(y_{b3} - y_{c2}\right) + F_{lb3y} = -m_{b3}g. \end{aligned} \tag{21}$$

Out race of bearing 4:

$$\begin{aligned} &m_{b4}\ddot{x}_{b4} + c_{hb4}\left(\dot{x}_{b4} - \dot{x}_{hb4}\right) + c_{bc4}\left(\dot{x}_{b4} - \dot{x}_{c2}\right) \\ &\quad + k_{bc4}\left(x_{b4} - x_{c2}\right) + F_{hb4x} = 0, \\ &m_{b4}\ddot{y}_{b4} + c_{hb4}\left(\dot{y}_{b4} - \dot{y}_{hb4}\right) + c_{bc4}\left(\dot{y}_{b4} - \dot{y}_{c2}\right) \\ &\quad + k_{bc4}\left(y_{b4} - y_{c2}\right) + F_{hb4y} = -m_{b4}g. \end{aligned} \tag{22}$$

Out race of bearing 6:

$$\begin{aligned} &m_{b6}\ddot{x}_{b6} + c_{lb6}\left(\dot{x}_{b6} - \dot{x}_{lb6}\right) + c_{bc6}\left(\dot{x}_{b6} - \dot{x}_{c3}\right) \\ &\quad + k_{bc6}\left(x_{b6} - x_{c3}\right) + F_{lb6x} = 0, \\ &m_{b6}\ddot{y}_{b6} + c_{lb6}\left(\dot{y}_{b6} - \dot{y}_{lb6}\right) + c_{bc6}\left(\dot{y}_{b6} - \dot{y}_{c3}\right) \\ &\quad + k_{bc6}\left(y_{b6} - y_{c3}\right) + F_{lb6y} = -m_{b6}g. \end{aligned} \tag{23}$$

Front casing:

$$\begin{aligned} &m_{c1}\ddot{x}_{c1} + c_{bc1}\left(\dot{x}_{c1} - \dot{x}_{b1}\right) + c_{12}\left(\dot{x}_{c1} - \dot{x}_{c2}\right) + c_{c1x}\dot{x}_{c1} \\ &\quad + k_{bc1}\left(x_{c1} - x_{b1}\right) + k_{12}\left(x_{c1} - x_{c2}\right) + k_{c1x}x_{c1} = 0, \\ &m_{c1}\ddot{y}_{c1} + c_{bc1}\left(\dot{y}_{c1} - \dot{y}_{b1}\right) + c_{12}\left(\dot{y}_{c1} - \dot{y}_{c2}\right) + c_{c1y}\dot{y}_{c1} \\ &\quad + k_{bc1}\left(y_{c1} - y_{b1}\right) + k_{12}\left(y_{c1} - x_{c2}\right) + k_{c1y}y_{c1} \\ &\quad = -m_{c1}g. \end{aligned} \tag{24}$$

Middle casing:

$$\begin{aligned} &m_{c2}\ddot{x}_{c2} + c_{bc2}\left(\dot{x}_{c2} - \dot{x}_{b2}\right) + c_{bc3}\left(\dot{x}_{c2} - \dot{x}_{b3}\right) \\ &\quad + c_{bc4}\left(\dot{x}_{c2} - \dot{x}_{b4}\right) + c_{12}\left(\dot{x}_{c2} - \dot{x}_{c1}\right) + c_{23}\left(\dot{x}_{c2} - \dot{x}_{c3}\right) \\ &\quad + c_{c2x}\dot{x}_{c2} + k_{bc2}\left(x_{c2} - x_{b2}\right) + k_{bc3}\left(x_{c2} - x_{b3}\right) \\ &\quad + k_{bc4}\left(x_{c2} - x_{b4}\right) + k_{12}\left(x_{c2} - x_{c1}\right) + k_{23}\left(x_{c2} - x_{c3}\right) \\ &\quad + k_{c2x}x_{c2} = 0, \\ &m_{c2}\ddot{y}_{c2} + c_{bc2}\left(\dot{y}_{c2} - \dot{y}_{b2}\right) + c_{bc3}\left(\dot{y}_{c2} - \dot{y}_{b3}\right) \\ &\quad + c_{bc4}\left(\dot{y}_{c2} - \dot{y}_{b4}\right) + c_{12}\left(\dot{y}_{c2} - \dot{y}_{c1}\right) + c_{23}\left(\dot{y}_{c2} - \dot{y}_{c3}\right) \\ &\quad + c_{c2y}\dot{y}_{c2} + k_{bc2}\left(y_{c2} - y_{b2}\right) + k_{bc3}\left(y_{c2} - y_{b3}\right) \\ &\quad + k_{bc4}\left(y_{c2} - y_{b4}\right) + k_{12}\left(y_{c2} - y_{c1}\right) + k_{23}\left(y_{c2} - y_{c3}\right) \\ &\quad + k_{c2y}y_{c2} = -m_{c2}g. \end{aligned} \tag{25}$$

Rear casing:

$$\begin{aligned} &m_{c3}\ddot{x}_{c3} + c_{bc6}\left(\dot{x}_{c3} - \dot{x}_{b6}\right) + c_{23}\left(\dot{x}_{c3} - \dot{x}_{c2}\right) + c_{c3x}\dot{x}_{c3} \\ &\quad + k_{bc6}\left(x_{c3} - x_{b6}\right) + k_{23}\left(x_{c3} - x_{c2}\right) + k_{c3x}x_{c3} = 0, \\ &m_{c3}\ddot{y}_{c3} + c_{bc6}\left(\dot{y}_{c3} - \dot{y}_{b6}\right) + c_{23}\left(\dot{y}_{c3} - \dot{y}_{c2}\right) + c_{c3y}\dot{y}_{c3} \\ &\quad + k_{bc6}\left(y_{c3} - y_{b6}\right) + k_{23}\left(y_{c3} - y_{c2}\right) + k_{c3y}y_{c3} = -m_{c3}g. \end{aligned} \tag{26}$$

where the bearing forces of bearings 1–6 are linear models, and no nonlinear factors are involved. The specific formulas are shown in Appendix.

4. Theoretical Simulation

For dual-rotor systems, there are two types of operating conditions: primary excitation from high-pressure rotor and from low-pressure rotor. In this section, the vibration transfer characteristics of the system under the two conditions are calculated and discussed. The high-pressure primary excitation corresponds to the constant speed of the low-pressure rotor and the rising speed of the high-pressure rotor in engineering. The case of low-pressure primary excitation is where the speed of the high-pressure rotor is constant and that of the low-pressure rotor is increased. The vibration equations of the dual-rotor system are solved numerically by the Newmark method. The parameters of the dual-rotor system are shown in Table 1.

4.1. Beat Vibration. The dual-rotor model has two excitations from high- and low-pressure rotors' imbalance. If the excitation frequency of the low-pressure rotor is close to that of the high-pressure rotor, according to the vibration theory of double-frequency excitation, the steady-state response of the dual-rotor system is exhibited as a beat vibration. The beat vibration of rotors was revealed in Reference [20]. But how is the appearance of such vibration on the casing? In this simulation, the vibration acceleration response of middle section on casing is calculated as shown in Figure 3 under four speed combinations. The speed combinations are $\omega_h = 125$, $\omega_l = 80$; $\omega_h = 125$, $\omega_l = 105$; $\omega_h = 150$, $\omega_l = 125$; and $\omega_h = 200$, $\omega_l = 125$.

The results show that when the two excitation speeds are close, the vibration of the casing will also appear as the phenomenon of beat vibration, as shown in Figures 3(b) and 3(c). If the two frequencies are far away, the beat vibration disappears, as shown in Figures 3(a) and 3(d).

Table 1: Main parameters of the dual-rotor-casing system.

Dynamic parameter (unit)	Value
Mass of high-pressure rotor, m_{hd} (kg)	5
Mass of low-pressure rotor 1, m_{ld1} (kg)	1.5
Mass of low-pressure rotor 2, m_{ld2} (kg)	2.5
Stiffness of high-pressure rotor shaft, k_{hs} (N/m)	1×10^7
Stiffness of low-pressure rotor shaft 1, k_{l1} (N/m)	1×10^7
Stiffness of low-pressure rotor shaft 2, k_{l2} (N/m)	1×10^7
Support stiffness between front casing and base, k_{c1} (N/m)	1×10^9
Support stiffness between middle casing and base, k_{c2} (N/m)	1×10^9
Support stiffness between rear casing and base, k_{c3} (N/m)	1×10^9
Support damping between front casing and base, c_{c1} (N·s/m)	1500
Support damping between middle casing and base, c_{c2} (N·s/m)	1500
Support damping between rear casing and base, c_{c3} (N·s/m)	1500

4.2. Evaluation Index. According to the support and force transmission structure of the rotor system, the main vibration measurement section on casing is determined as front, middle, and rear sections. The vibration evaluation indexes of these sections proposed in Section 2.2 are calculated based on the dynamic response of the established dual-rotor-casing model.

Firstly, the rotating speed of high-pressure rotor increases, keeping that of the low-pressure rotor constant as 125 rad/s. The vibration transmissibility of the high-pressure rotor to the three vibration measurement sections are shown in Figure 4. At low speeds, the vibration transmissibility remains almost unchanged, but when the rotating speed is higher than 920 rad/s, the transmissibility decreases rapidly. It shows that the transmission of high-pressure rotor vibration to the vibration measurement section is band-pass in low-speed interval; that is, more vibration of the rotor can reach the corresponding vibration measurement section on the casing, and the section can reflect the vibration of high-pressure rotor effectively. In the case of high speed, the

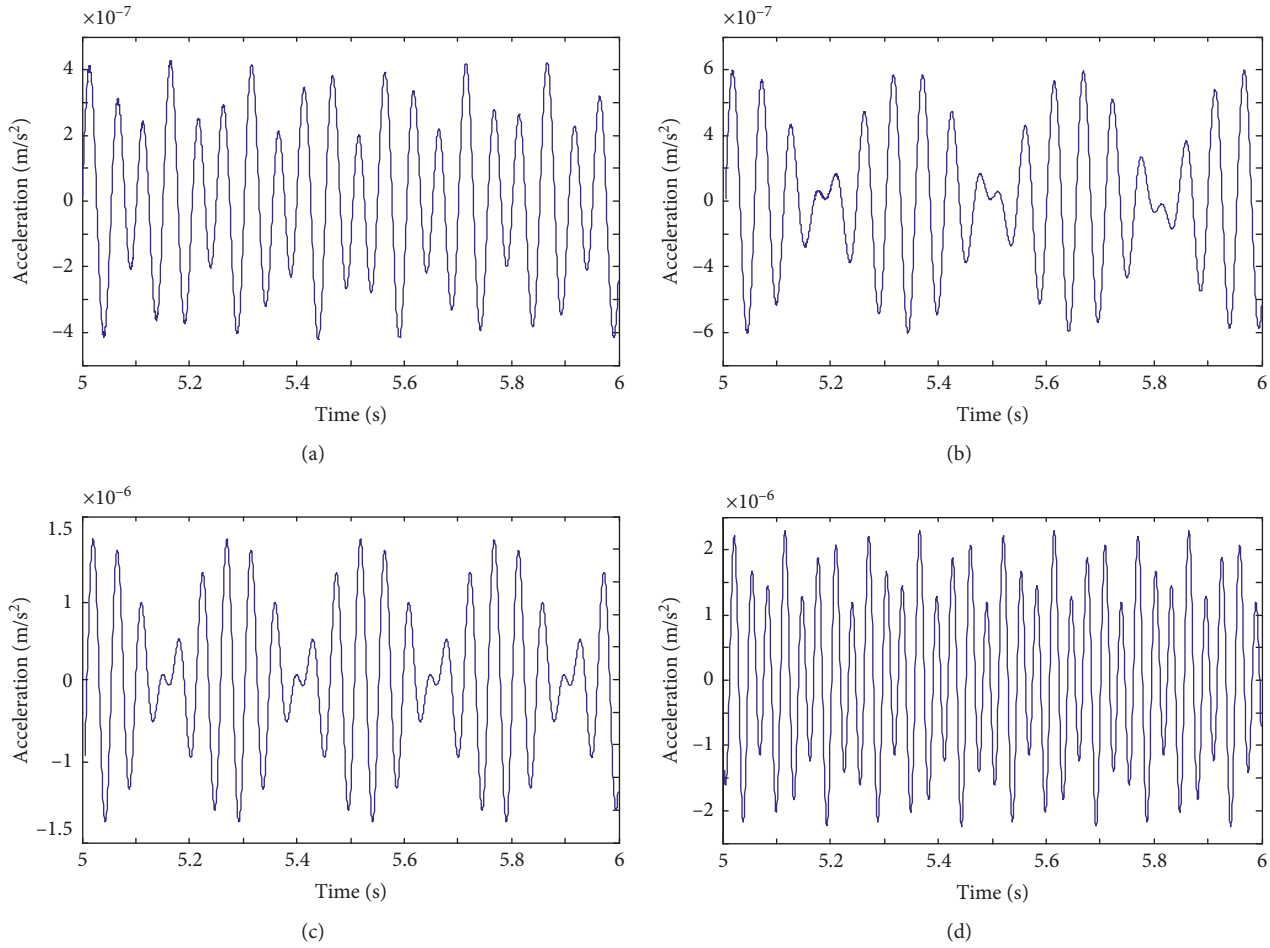

FIGURE 3: Beat vibration waveforms of middle measurement section on casing at different rotating speeds: (a) $\omega_h = 125$ rad/s, $\omega_l = 80$ rad/s, (b) $\omega_h = 125$ rad/s, $\omega_l = 105$ rad/s, (c) $\omega_h = 150$ rad/s, $\omega_l = 125$ rad/s, and (d) $\omega_h = 200$ rad/s, $\omega_l = 125$ rad/s.

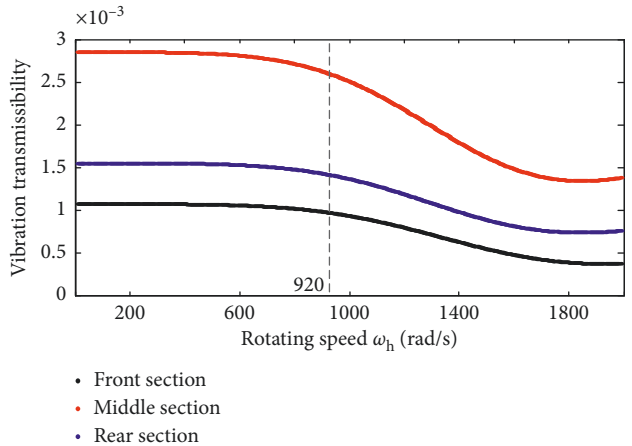

FIGURE 4: Vibration transmissibility ξ with varying rotating speed of high-pressure rotor ω_h: front section (black), middle section (red), and rear section (blue).

vibration of high-pressure rotor is less transferred to the casing with a low vibration transmissibility. The speed interval is called band-stop interval, where the vibration measurement section reflects the vibration of high-pressure rotor slightly. Furthermore, the vibration transmissibility of the high-pressure rotor to each vibration measurement section is ranked as middle section > rear section > front section in the whole speed interval.

Figure 5 shows the vibration energy transmissibility from the high-pressure rotor to the three vibration sections. The value of the energy transmissibility is relatively high at lower rotational speeds and rapidly decreases when the speed is above 100 rad/s. It is consistent with the trend of vibration transmissibility, as band-pass at low speed and band-stop at high speed. The energy transmissibility of the high-pressure rotor to the middle section is highest among the three sections in the entire calculated speed interval. When the speed is lower than 100 rad/s, the energy transmissibility order of the three sections is middle section > front section > rear section. The vibration energy of the low-pressure rotor is bigger than that of the high-pressure rotor, which results the higher vibration energy of front section. Once the speed of the high-pressure rotor is above 100 rad/s, the order is changed as middle point > rear point > front point.

In addition, the energy transmissibility has a value jump when the speed of the high-pressure rotor is close to 125 rad/s which is the speed of the low-pressure rotor. This is because

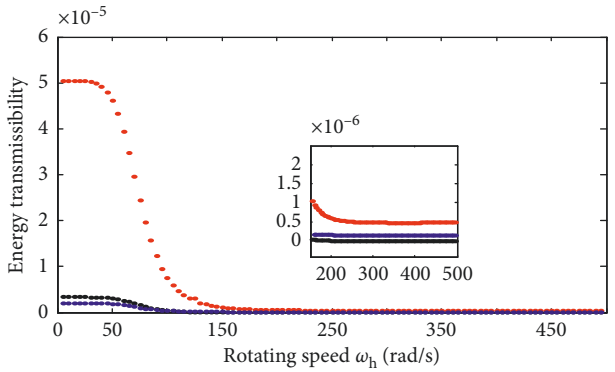

Figure 5: Energy transmissibility η with varying rotating speed of high-pressure rotor ω_h: front section (black), middle section (red), and rear section (blue).

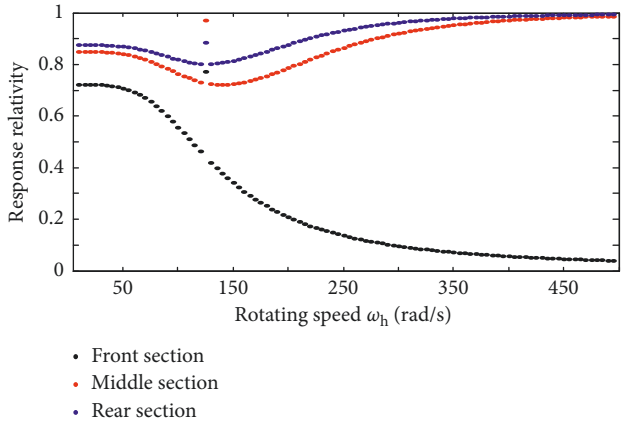

Figure 6: Response relativity R with varying rotating speed of high-pressure rotor ω_h: front section (black), middle section (red), and rear section (blue).

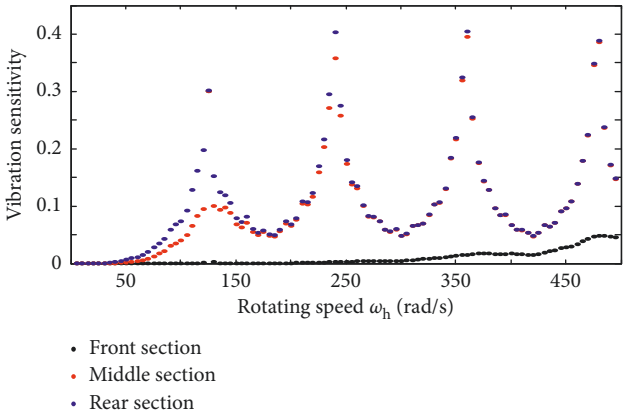

Figure 7: Vibration sensitivity S with varying rotating speed of high-pressure rotor ω_h: front section (black), middle section (red), and rear section (blue).

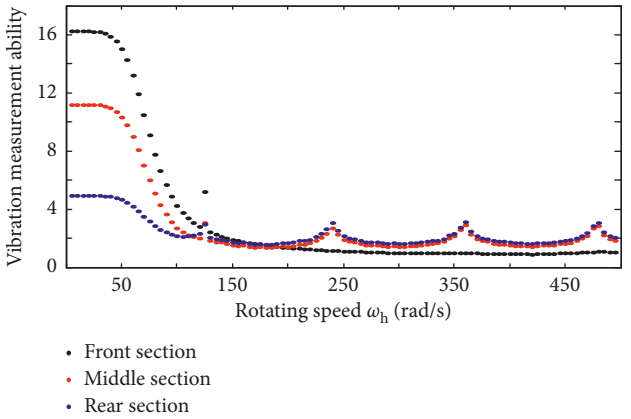

Figure 8: Vibration measurement ability C with varying rotating speed of high-pressure rotor ω_h: front section (black), middle section (red), and rear section (blue).

of the beat vibration, as shown in Figure 3. The vibration energy of the two rotors is enhanced, and the vibration energy transmitted to the casing is correspondingly increased.

Figure 6 reveals the response relativity of the high-pressure rotor to vibration measurement sections. In the whole speed interval, the relativity of the vibration response is ranked as rear section > middle section > front section. When the two rotors rotate at similar speeds, because of the beat vibration, the response relativity suddenly increases, and that of the middle section is the largest. Figure 7 shows the vibration sensitivity between the vibration measurement sections and the high-pressure rotor. The rear section has the lowest sensitivity at low speeds and the highest sensitivity at high speeds. When the speed of the high-pressure rotor is close to that of the low-pressure rotor, the value of the sensitivity jumps.

Figure 8 shows the variation of the comprehensive vibration measurement ability of the three vibration measurement sections calculated based on the above evaluation indexes. The weight coefficients are all set as 0.5 for simplification. The value of vibration measurement ability jumps because of beat vibration. When the speed of the high-pressure rotor is less than 175 rad/s, the vibration measurement ability is ranked as front section > middle section > rear section. When the speed is higher than 175 rad/s, the ability of front section is the lowest, and ability of the middle section almost equals to that of the rear section.

The variation of evaluation indexes of the three sections with the rotating speed of the low-pressure rotor increasing is shown in Figures 9–13, while the speed of the high-pressure rotor is fixed at 125 rad/s.

In this condition, the vibration transmissibility (Figure 9) is band-pass in the low-speed interval and band-stop in the high-speed interval. The order is middle section > rear section > front section. The highest value is 4.05×10^{-3}, which is slightly higher than that of the high-pressure rotor.

The value of energy transmissibility of the low-pressure rotor to the middle section is the highest (Figure 10) in the observed speed interval. When the speed of the low-pressure rotor is lower than 150 rad/s, the energy transmissibility to the rear measurement section is higher than that of the front section. The vibration energy of the high-pressure rotor is bigger than that of the low-pressure rotor, which results in

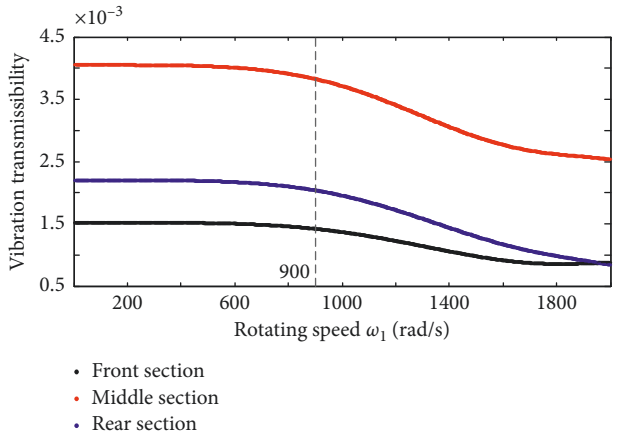

Figure 9: Vibration transmissibility ξ with varying rotating speed of low-pressure rotor ω_l: front section (black), middle section (red), and rear section (blue).

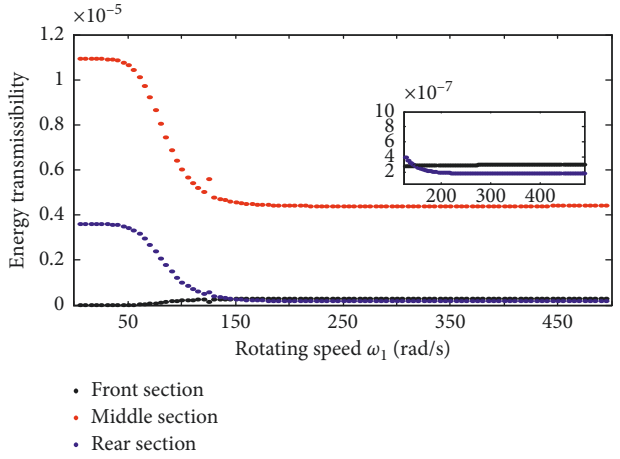

Figure 10: Energy transmissibility η with varying rotating speed of low-pressure rotor ω_l: front section (black), middle section (red), and rear section (blue).

the higher vibration energy of rear section. After the speed exceeds 150 rad/s, the energy transmissibility is ranked as middle point > front point > rear point. As the speed of the low-pressure rotor is close to that of high-pressure rotor 125 rad/s, the energy transmissibility has a jump because of the beat vibration.

Figure 11 shows the response relativity between the measurement sections and the low-pressure rotor. As the speed increases, the response relativity increases gradually. The response relativity of the middle measurement section is highest. When the rotation speed is 115 rad/s, the relativity of front section exceeds that of rear measurement section. There is a value jump beside the speed of 125 rad/s for beat vibration.

Figure 12 shows that the front section has the highest sensitivity to the low-pressure rotor vibration in the low speed interval. As the speed increases, the vibration sensitivity of the three sections tends to be uniform.

Figure 13 reveals the comprehensive vibration measurement ability of the three measurement sections. Before the speed of 120 rad/s, the ability order is rear section > middle

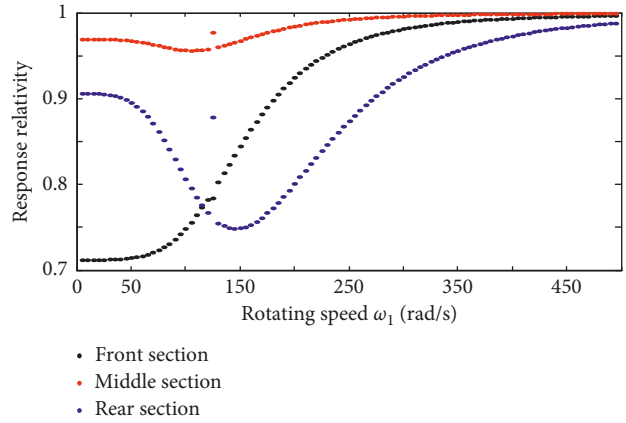

Figure 11: Response relativity R with varying rotating speed of low-pressure rotor ω_l: front section (black), middle section (red), and rear section (blue).

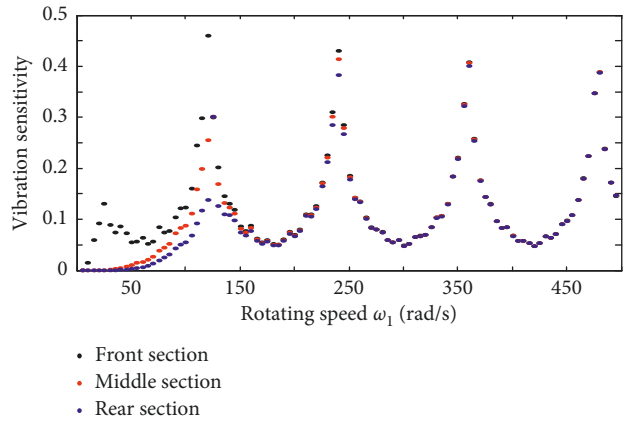

Figure 12: Vibration sensitivity S with varying rotating speed of low-pressure rotor ω_l: front section (black), middle section (red), and rear section (blue).

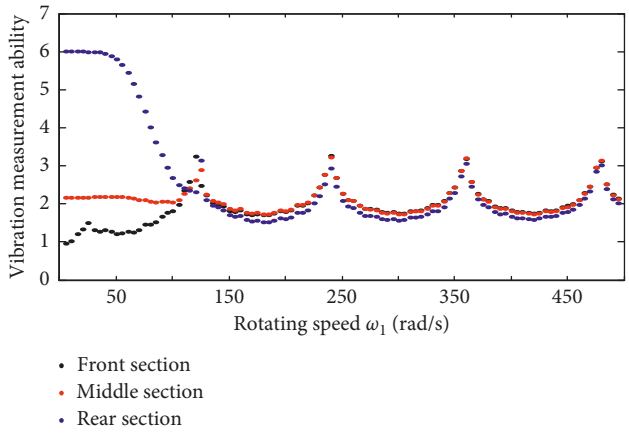

Figure 13: Vibration measurement ability C with varying rotating speed of low-pressure rotor ω_l: front section (black), middle section (red), and rear section (blue).

section > front section. When the speed exceeds 120 rad/s, the comprehensive vibration measurement ability of the three sections tends similar, and the middle section has a slightly higher ability than the other.

Considering the overall evaluation indexes of the three vibration measurement sections under the two types of rotor excitation, it can be found that the total vibration measurement ability of middle section is better than the others, followed by the rear section, and the front section has lowest ability. If the on-board vibration measurement section needs to be selected, the middle section is prioritized. The result is consistent with the application in engineering while the on-board measurement locations are just arranged on the middle section, which indicates the effectiveness of the proposed method.

5. Experimental Verification

Taking a certain type of aeroengine as a reference and corresponding to the dual-rotor-casing system model established in the simulation analysis of this paper, a pneumatic-driven aeroengine double-rotor-casing test bench is designed, as shown in Figure 14. The specific internal structure of the bench is consistent with the model in Section 3, as is illustrated in the cutaway view (Figure 14(b)). The vibration data of the casing under two kinds of operation conditions are collected. The evaluation indexes proposed in this paper are calculated, and the measurement ability of sections is summarized. The first operation condition is that the low-pressure rotor has a fixed rotational speed, while the high-pressure rotor takes a number of rotating speeds. And the second condition is that the high-pressure rotor has a fixed speed, while the low-pressure rotor takes several speeds, respectively.

5.1. Experimental Configuration. The configuration of the test bench is shown in Figure 14. The front, middle, and rear vibration measurement sections acquired in simulation are also used for experimental measurement. They are located on the support sections of the corresponding rotors on casing, and accelerometers are installed at these sections for vibration measurement. Compressed gas is used to drive the high- and low-pressure turbines to provide power for the system. The support structure is the same as a certain engine and the system dynamics model established in this paper.

5.2. Analysis and Discussion. In the experiment, experimental data are collected according to two types of operation conditions, and each vibration measurement evaluation index is calculated. Figure 15 shows the beat vibration phenomenon when the speeds of high- and low-pressure rotors are similar in the experiment, which corresponds to the simulation response well.

Figures 16–20 show the vibration transmissibility, energy transmissibility, response relativity, vibration sensitivity, and vibration measurement ability when the speed of high-pressure rotor takes 21 Hz, 30 Hz, 41 Hz, 49 Hz, 60 Hz, 70 Hz, and 79 Hz, respectively, and the speed of the low-pressure rotor is 20 Hz.

The vibration transmissibility (Figure 16) of the middle measurement section is the highest, followed by the rear section, and the transmissibility of the front section is the lowest. The value of energy transmissibility (Figure 17) has a downtrend along with the increasing speed. The order of the three sections is middle section > rear section > front section.

In terms of the response relativity between the vibration measurement sections and the high-pressure rotor (Figure 18), the value of the middle measurement section and the rear section is basically equal at low speeds. The value of the front section is lower. As the speed increases, the relativity of the front section exceeds that of the rear section.

Figure 19 shows the vibration sensitivity of the vibration measurement sections to the high-pressure rotor. The sensitivity of the rear section is the highest in observed speed interval, and the value of the three sections increases with the increase of the rotating speed. The front section has the lowest sensitivity.

The comprehensive vibration measurement ability of the three measurement sections is calculated and shown in Figure 20. When the high-pressure rotor takes low speed, the value of the vibration measurement ability of each section is higher. As the speed increases, the comprehensive vibration measurement ability decreases.

In the second type of operation conditions, the rotating speed of the high-pressure rotor is fixed at 20 Hz, and the speed of the low-pressure rotor takes 19 Hz, 30 Hz, 40 Hz, 50 Hz, 60 Hz, 69 Hz, and 81 Hz, respectively. The vibration evaluation indexes are calculated and illustrated in Figures 21–25.

As the speed of low-pressure rotor increases, the vibration transmissibility and energy transmissibility decrease gradually. The value of the middle measurement section is relatively higher. The value of the response relativity between the middle section and the low-pressure rotor is the highest, and the vibration sensitivity of the rear section to the low-pressure rotor is the highest. On the comprehensive vibration measurement ability of the three sections, the ability of the rear measurement section in the low-speed interval is the higher. As the speed increases, the value of the middle section and the front section increases.

From each vibration evaluation index of the three measurement sections under two conditions, the middle vibration measurement section has the best performance, followed by the rear section, and the front section is the last one. Both the variation trend and value order of the evaluation indexes of the three sections from experiments agree with those of simulation. The values of the evaluation indexes from experiments are slightly lower than that of simulation because of complex interference from other components of the test bench. The experimental results can give a quantitatively and qualitatively verification to the theoretical analysis and demonstrate the effectiveness of the evaluation method proposed in this paper further.

6. Conclusion

An evaluation method of vibration measurement on casing for the aeroengine rotor-casing system is proposed, aiming at the requirement of monitoring vibration of rotors in the

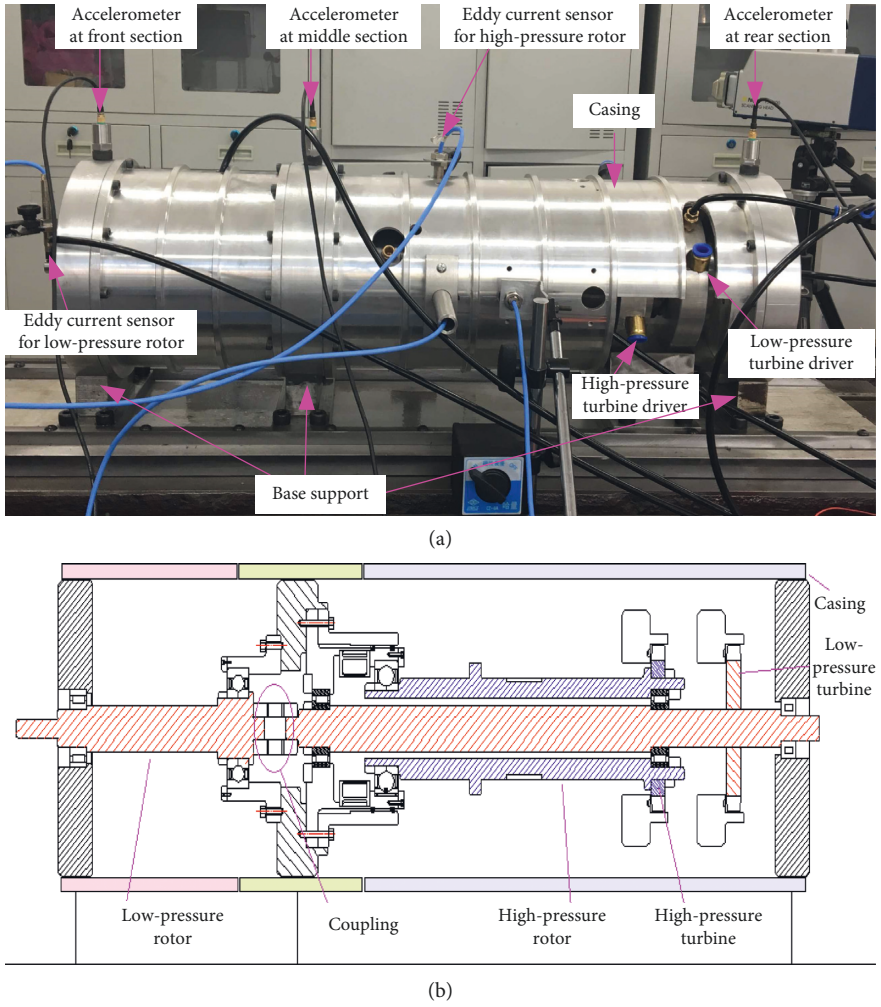

Figure 14: Dual-rotor-casing rig. (a) Test layout and (b) cutaway view.

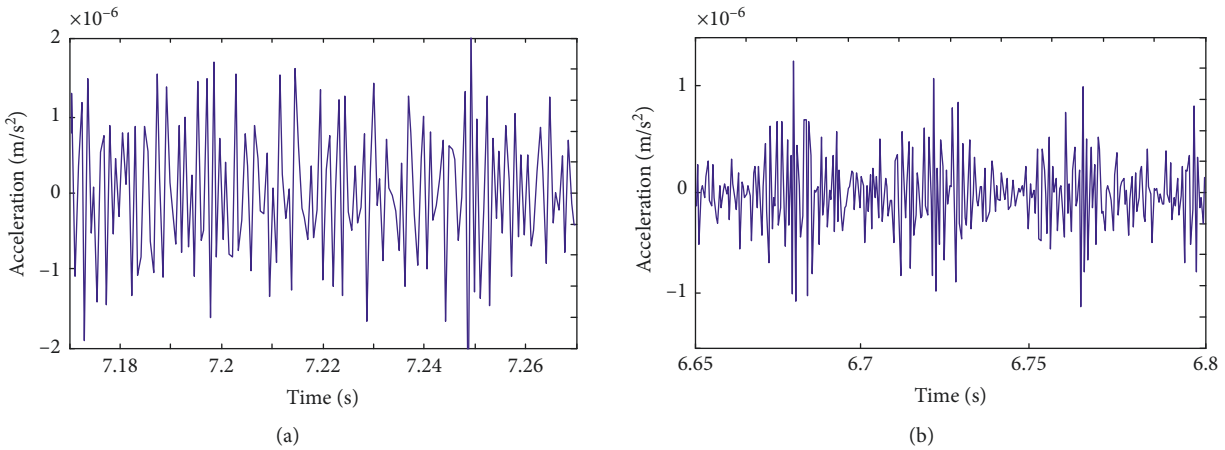

Figure 15: Continued.

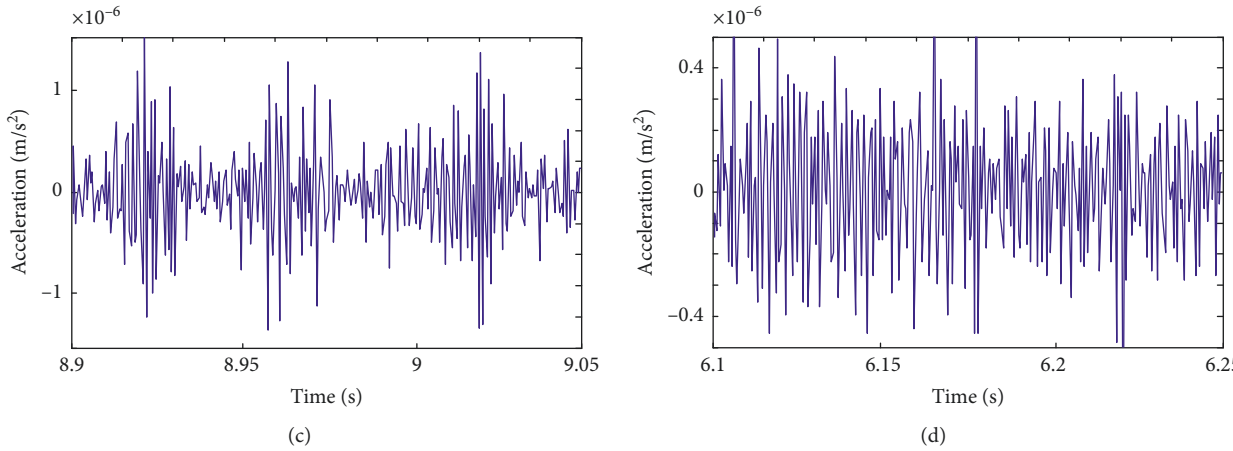

Figure 15: Experimental beat vibration waveforms of middle measurement section on casing at different rotating speeds: (a) $\omega_h = 125$ rad/s, $\omega_l = 80$ rad/s, (b) $\omega_h = 125$ rad/s, $\omega_l = 105$ rad/s, (c) $\omega_h = 150$ rad/s, $\omega_l = 125$ rad/s, and (d) $\omega_h = 200$ rad/s, $\omega_l = 125$ rad/s.

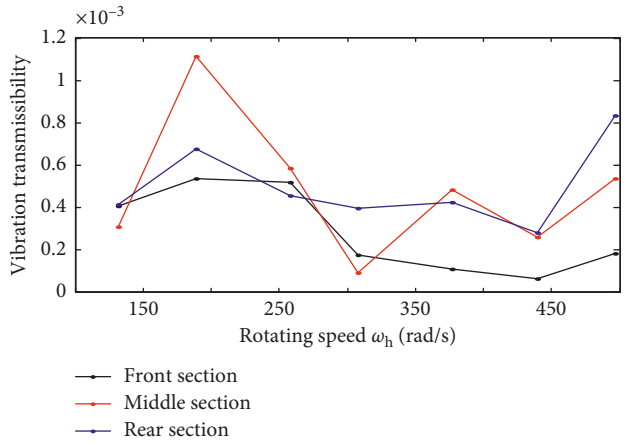

Figure 16: Experimental vibration transmissibility ξ with varying rotating speed of high-pressure rotor ω_h: front section (black), middle section (red), and rear section (blue).

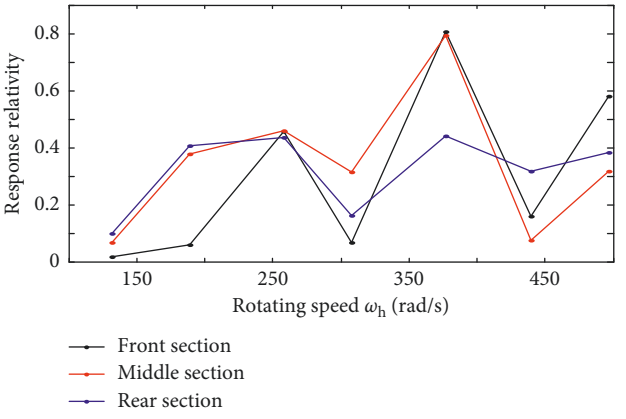

Figure 18: Experimental response relativity R with varying rotating speed of high-pressure rotor ω_h: front section (black), middle section (red), and rear section (blue).

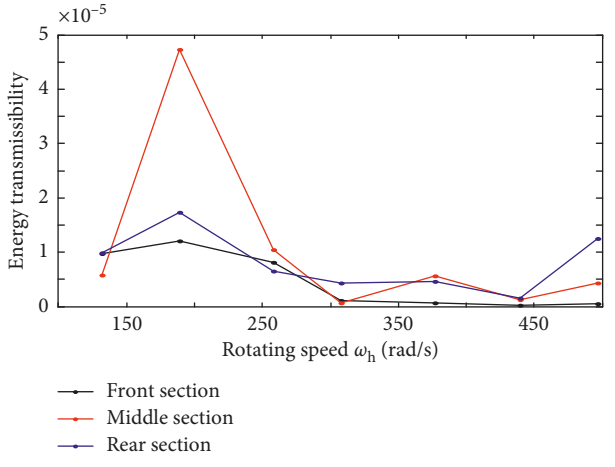

Figure 17: Experimental energy transmissibility η with varying rotating speed of high-pressure rotor ω_h: front section (black), middle section (red), and rear section (blue).

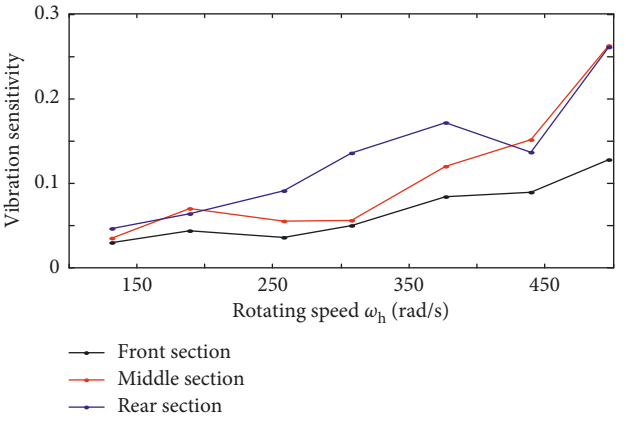

Figure 19: Experimental vibration sensitivity S with varying rotating speed of high-pressure rotor ω_h: front section (black), middle section (red), and rear section (blue).

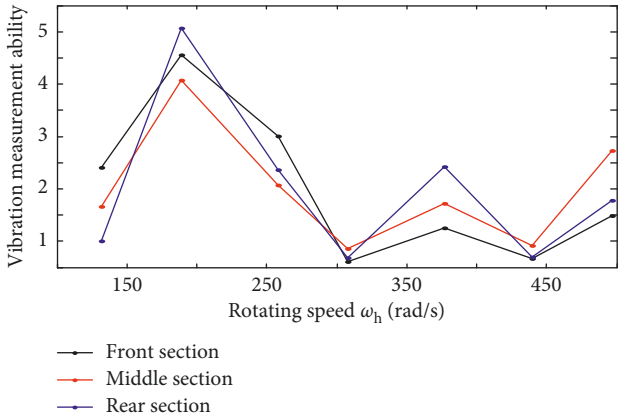

Figure 20: Experimental vibration measurement ability C with varying rotating speed of high-pressure rotor ω_h: front section (black), middle section (red), and rear section (blue).

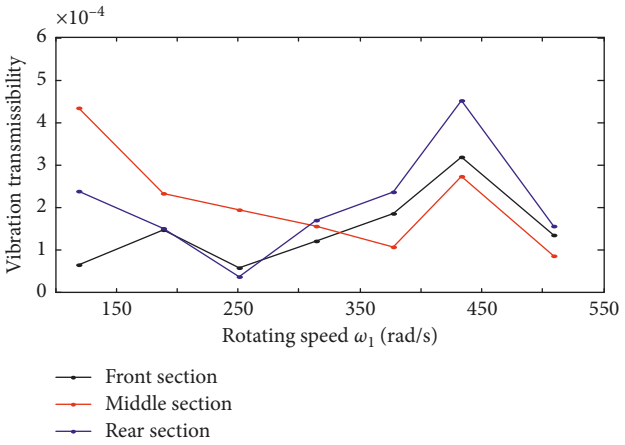

Figure 21: Experimental vibration transmissibility ξ with varying rotating speed of low-pressure rotor ω_l: front section (black), middle section (red), and rear section (blue).

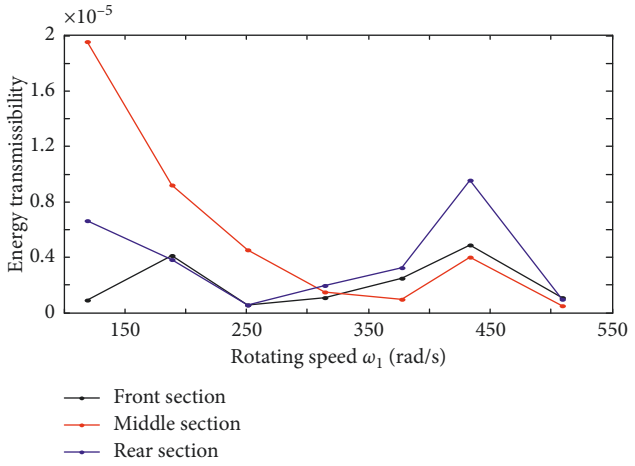

Figure 22: Experimental energy transmissibility η with varying rotating speed of low-pressure rotor ω_l: front section (black), middle section (red), and rear section (blue).

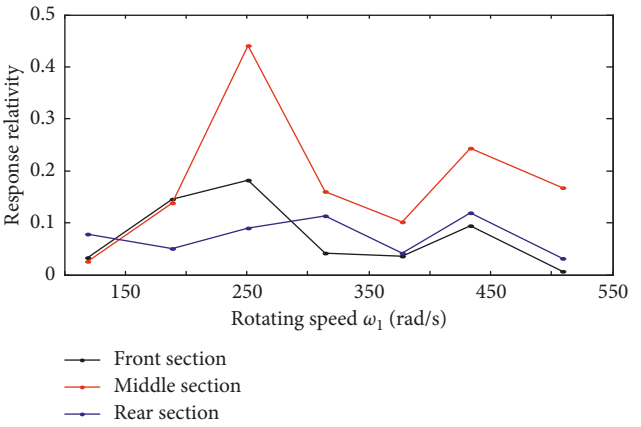

Figure 23: Experimental response relativity R with varying rotating speed of low-pressure rotor ω_l: front section (black), middle section (red), and rear section (blue).

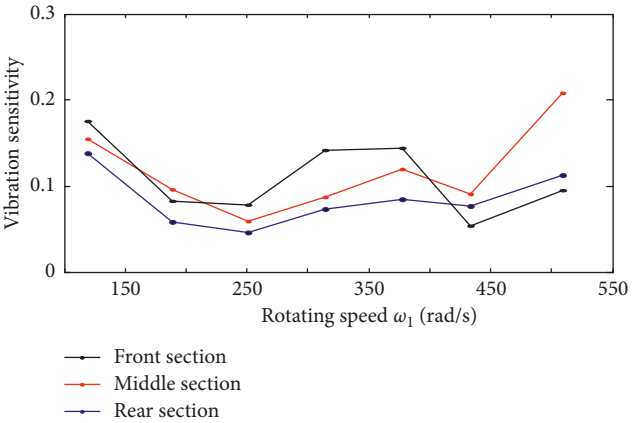

Figure 24: Experimental vibration sensitivity S with varying rotating speed of low-pressure rotor ω_l: front section (black), middle section (red), and rear section (blue).

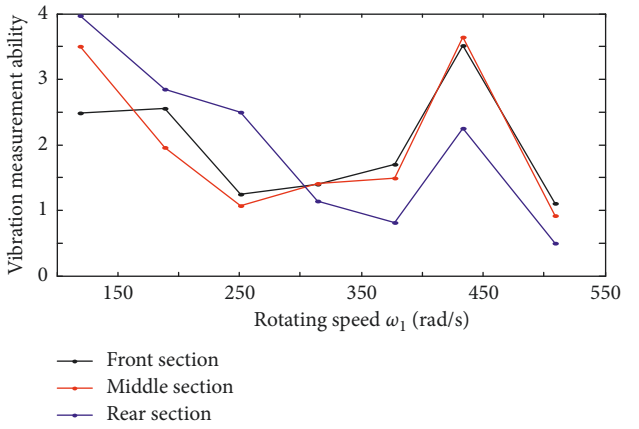

Figure 25: Experimental vibration measurement ability C with varying rotating speed of low-pressure rotor ω_l: front section (black), middle section (red), and rear section (blue).

vibration measurement of aeroengine. A series of evaluation indexes are defined, including vibration transmissibility, energy transmissibility, response relativity, vibration sensitivity, and comprehensive vibration measurement ability.

According to a certain aeroengine configuration, the dynamic model of a dual-rotor-casing system with intermediate bearings is established, and a pneumatic-driven dual-rotor-casing test bench with the same support structure is designed. The focus and correlation of the front, middle, and rear measurement sections in reflecting the vibration of the high- and low-pressure rotors are comprehensively analyzed and sound verified through simulation and experiment.

The comprehensive vibration measurement performance of the middle measurement section is the best, followed by rear section and front section. Thus, the middle section is the preferred installation section for the on-board measurement, which is consistent with the location of measurement section on-board of this type of engine in engineering.

The results from experiment and location of on-board vibration measurement validate the effectiveness and applicability of the proposed evaluation method. Meanwhile, the results illustrate the rationality of the three sections for vibration measurement on casing in engineering. The overall work provides a method for evaluating the vibration relation between casing and rotors and can be a reference for transducer optimization of the dual-rotor-casing system.

Appendix

$$
\begin{aligned}
F_{\mathrm{lb}1x} &= k_{\mathrm{b}1}\left(x_{\mathrm{lb}1} - x_{\mathrm{b}1}\right) + c_{\mathrm{b}1}\left(\dot{x}_{\mathrm{lb}1} - \dot{x}_{\mathrm{b}1}\right),\\
F_{\mathrm{lb}1y} &= k_{\mathrm{b}1}\left(y_{\mathrm{lb}1} - y_{\mathrm{b}1}\right) + c_{\mathrm{b}1}\left(\dot{y}_{\mathrm{lb}1} - \dot{y}_{\mathrm{b}1}\right),\\
F_{\mathrm{lb}2x} &= k_{\mathrm{b}2}\left(x_{\mathrm{lb}2} - x_{\mathrm{b}2}\right) + c_{\mathrm{b}2}\left(\dot{x}_{\mathrm{lb}2} - \dot{x}_{\mathrm{b}2}\right),\\
F_{\mathrm{lb}2y} &= k_{\mathrm{b}2}\left(y_{\mathrm{lb}2} - y_{\mathrm{b}2}\right) + c_{\mathrm{b}1}\left(\dot{y}_{\mathrm{lb}2} - \dot{y}_{\mathrm{b}2}\right),\\
F_{\mathrm{lb}3x} &= k_{\mathrm{b}3}\left(x_{\mathrm{lb}3} - x_{\mathrm{b}3}\right) + c_{\mathrm{b}3}\left(\dot{x}_{\mathrm{lb}3} - \dot{x}_{\mathrm{b}3}\right),\\
F_{\mathrm{lb}3y} &= k_{\mathrm{b}3}\left(y_{\mathrm{lb}3} - y_{\mathrm{b}3}\right) + c_{\mathrm{b}3}\left(\dot{y}_{\mathrm{lb}3} - \dot{y}_{\mathrm{b}3}\right),\\
F_{\mathrm{hb}4x} &= k_{\mathrm{b}4}\left(x_{\mathrm{hb}4} - x_{\mathrm{b}4}\right) + c_{\mathrm{b}4}\left(\dot{x}_{\mathrm{hb}4} - \dot{x}_{\mathrm{b}4}\right),\\
F_{\mathrm{hb}4y} &= k_{\mathrm{b}4}\left(y_{\mathrm{hb}4} - y_{\mathrm{b}4}\right) + c_{\mathrm{b}4}\left(\dot{y}_{\mathrm{hb}4} - \dot{y}_{\mathrm{b}4}\right),\\
F_{\mathrm{lb}5x} &= k_{\mathrm{b}5}\left(x_{\mathrm{lb}4} - x_{\mathrm{hb}5}\right) + c_{\mathrm{b}5}\left(\dot{x}_{\mathrm{lb}5} - \dot{x}_{\mathrm{hb}5}\right),\\
F_{\mathrm{lb}5y} &= k_{\mathrm{b}5}\left(y_{\mathrm{lb}4} - y_{\mathrm{hb}5}\right) + c_{\mathrm{b}5}\left(\dot{y}_{\mathrm{lb}5} - \dot{y}_{\mathrm{hb}5}\right),\\
F_{\mathrm{lb}6x} &= k_{\mathrm{b}6}\left(x_{\mathrm{lb}6} - x_{\mathrm{b}6}\right) + c_{\mathrm{b}6}\left(\dot{x}_{\mathrm{lb}6} - \dot{x}_{\mathrm{b}6}\right),\\
F_{\mathrm{lb}6y} &= k_{\mathrm{b}6}\left(y_{\mathrm{lb}6} - y_{\mathrm{b}6}\right) + c_{\mathrm{b}6}\left(\dot{y}_{\mathrm{lb}6} - \dot{y}_{\mathrm{b}6}\right),
\end{aligned}
\tag{A.1}
$$

where $k_{\mathrm{b}1}$, $k_{\mathrm{b}2}$, $k_{\mathrm{b}3}$, $k_{\mathrm{b}4}$, $k_{\mathrm{b}5}$, $k_{\mathrm{b}6}$, $c_{\mathrm{b}1}$, $c_{\mathrm{b}2}$, $c_{\mathrm{b}3}$, $c_{\mathrm{b}4}$, $c_{\mathrm{b}5}$, and $c_{\mathrm{b}6}$ are support stiffness and damping of bearings.

Data Availability

No data were used to support this study.

Conflicts of Interest

There are no conflicts of interest.

Acknowledgments

The work was supported by the 973 Program of China (no. 2015CB057400) and the National Natural Science Foundation of China (no. 11672201).

References

[1] J. A. Keller and P. Grabill, "Inserted fault vibration monitoring tests for a CH-74D AFT swashplate bearing," in *Proceedings of 61st American Helicopter Society Annual Forum 2005*, pp. 151–160, Grapevine, TX, USA, June 2005.

[2] D. Wroblewski and P. Grabill, "Analysis of gas turbine vibration signals for augmentor fault detection," in *Proceedings of 7th Joint Propulsion Conference and Exhibit*, Salt Lake City, UT, USA, July 2001.

[3] X. Su, S. Wang, D. Zhu, and J. Shi, "Harmonic analysis and optimized vibration sensor locations of the helicopter intermediate gearbox," *Journal of Beijing University of Aeronautics and Astronautics*, vol. 37, no. 9, pp. 1049–1053, 2011.

[4] H. Qin, K. Xu, and L. Jiang, "Research on distribution of airborne vibration monitoring measuring points for the aeroengine," *Journal of Propulsion Technology*, vol. 28, no. 6, pp. 697–702, 2007.

[5] Y. Ouyang, P. He, and Z. Liu, "Investigation of the optimization method of the vibration transducer layout of aero engine," *Turbine Technology*, vol. 60, no. 5, pp. 359–362, 2018.

[6] Y. Wang, Z. Zhang, M. Liao, and P. Yu, "Section selecting for engine vibration measurement based on dynamic analysis," *Journal of Aerospace Power*, vol. 33, no. 6, pp. 1446–1455, 2018.

[7] C. Papadimitriou, "Optimal sensor placement methodology for parametric identification of structural systems," *Journal of Sound and Vibration*, vol. 278, no. 4-5, pp. 923–947, 2004.

[8] D. Hochmann, E. Limoge, E. Bechhoefer, and D. Cihlar, "Surface roughness and vibration study of an accelerometer mount used in a helicopter health usage and management system," in *Proceedings of IEEE Aerospace Conference*, Big Sky, MT, USA, March 2002.

[9] D. S. Li, H. N. Li, and C. P. Fritzen, "On optimal sensor placement criterion for structural health monitoring with representative least squares method," *Key Engineering Materials*, vol. 413-414, pp. 383–391, 2009.

[10] A. P. Cherng, "Optimal sensor placement for modal parameter identification using signal subspace correlation techniques," *Mechanical Systems and Signal Processing*, vol. 17, no. 2, pp. 361–378, 2003.

[11] Z. Y. Shi, S. S. Law, and L. M. Zhang, "Optimum sensor placement for StructuralDamage detection," *Journal of Engineering Mechanics*, vol. 126, no. 11, pp. 1173–1179, 2000.

[12] H. Guo, L. Zhang, L. Zhang, and J. Zhou, "Optimal placement of sensors for structural health monitoring using improved genetic algorithms," *Smart Materials and Structures*, vol. 13, no. 4, pp. 528–534, 2004.

[13] K. Worden and A. P. Burrows, "Optimal sensor placement for fault detection," *Engineering Structures*, vol. 23, no. 8, pp. 885–901, 2001.

[14] M. D. Sensmeier and K. L. Nichol, "Optimum placement of sensors for vibration measurements on turbine engine blades," in *Proceedings of 39th AIAA/ASME/ASCE/AHS/ASC Structures, Structural Dynamics, and Materials Conference and Exhibit*, Long Beach, CA, USA, April 1998.

[15] J. Xu, Y. Wang, and L. Xu, "PHM-oriented sensor optimization selection based on multiobjective model for aircraft

engines," *IEEE Sensors Journal*, vol. 15, no. 9, pp. 4836–4844, 2015.

[16] N. Najjar, S. Gupta, J. Hare, S. Kandil, and R. Walthall, "Optimal sensor selection and fusion for heat exchanger fouling diagnosis in aerospace systems," *IEEE Sensors Journal*, vol. 16, no. 12, pp. 4866–4881, 2016.

[17] U. Tapken and L. Enghardt, "Optimization of sensor arrays for radial mode analysis in flow ducts," in *Proceedings of 12th AIAA/CEAS Aeroacoustics Conference*, Cambridge, MA, USA, May 2006.

[18] L. Liu, X. Liang, and M. J. Zuo, "Vibration signal modeling of a planetary gear set with transmission path effect analysis," *Measurement*, vol. 85, pp. 20–31, 2016.

[19] H. Xiao, X. Zhou, J. Liu, and Y. Shao, "Vibration transmission and energy dissipation through the gear-shaft-bearing-housing system subjected to impulse force on gear," *Measurement*, vol. 102, pp. 64–79, 2017.

[20] Y. Yang, D. Cao, T. Yu, D. Wang, and C. Li, "Prediction of dynamic characteristics of a dual-rotor system with fixed point rubbing-theoretical analysis and experimental study," *International Journal of Mechanical Sciences*, vol. 115-116, pp. 253–261, 2016.